

Valley-polarized quantum anomalous Hall effect in van der Waals heterostructures based on monolayer jacutingaite family materials

Xudong Zhu^{§,1,2} Yuqian Chen^{§,1,2} Zheng Liu,^{1,2,*} Yulei Han,^{3,†} and Zhenhua Qiao^{1,2,‡}

¹*ICQD, Hefei National Research Center for Physical Sciences at the Microscale, University of Science and Technology of China, Hefei, Anhui 230026, China*

²*CAS Key Laboratory of Strongly-Coupled Quantum Matter Physics, and Department of Physics, University of Science and Technology of China, Hefei, Anhui 230026, China*

³*Department of Physics, Fuzhou University, Fuzhou, Fujian 350108, China*

(Dated: November 28, 2022)

We numerically study the general valley polarization and anomalous Hall effect in van der Waals (vdW) heterostructures based on monolayer jacutingaite family materials Pt_2AX_3 ($A = \text{Hg, Cd, Zn}$; $X = \text{S, Se, Te}$). We perform a systematic study on the atomic, electronic, and topological properties of vdW heterostructures composed of monolayer Pt_2AX_3 and two-dimensional ferromagnetic insulators. We show that four kinds of vdW heterostructures exhibit valley-polarized quantum anomalous Hall phase, i.e., $\text{Pt}_2\text{HgS}_3/\text{NiBr}_2$, $\text{Pt}_2\text{HgSe}_3/\text{CoBr}_2$, $\text{Pt}_2\text{HgSe}_3/\text{NiBr}_2$, and $\text{Pt}_2\text{ZnS}_3/\text{CoBr}_2$, with a maximum valley splitting of 134.2 meV in $\text{Pt}_2\text{HgSe}_3/\text{NiBr}_2$ and sizable global band gap of 58.8 meV in $\text{Pt}_2\text{HgS}_3/\text{NiBr}_2$. Our findings demonstrate an ideal platform to implement applications on topological valleytronics.

I. INTRODUCTION

The honeycomb lattice materials, such as graphene [1–4] and transition metal dichalcogenides (TMDs) [5–7], host two inequivalent valleys K and K' in momentum space located at the corners of the hexagonal Brillouin zone. In addition to the spin of electron, valley is another degree of freedom in two-dimensional honeycomb-like materials. The valley degree of freedom can be tuned by electric fields [8–10], external magnetic fields [11–13], and circularly polarized light excitation [14–16]. Similar to spintronics, valleytronics is mainly focused on manipulating valley degree of freedom in designing functional nanodevices [17–20], such as electron beam splitter, valley filter, and valley valves [21–25].

Quantum anomalous Hall effect (QAHE) is the quantized version of Hall effect without applying external magnetic fields [26–29], and has been experimentally realized in various material systems [30–33]. The valley polarization, e.g., in TMD materials, is often topologically trivial [34–37], whereas QAHE is usually a valley degenerated state. To implement valley-polarized QAHE, the inversion symmetry and time-reversal symmetry should be simultaneously broken. One rational way to realize valley-polarized QAHE is by inducing the magnetic proximity effect in the \mathbb{Z}_2 topological insulator/ferromagnetic insulator heterostructures [38–43]. Although several valley-polarized QAHE systems have been theoretically proposed [38–47], more experimentally realizable candidates are still highly desired to observe the valley-polarized QAHE.

In this article, we propose an ideal platform to realize valley polarization and valley-polarized QAHE based

on monolayer jacutingaite family materials. Jacutingaite (Pt_2HgSe_3) is a natural mineral with large intrinsic spin-orbit coupling (SOC). The atomic structure of jacutingaite can be treated as a quarter of X atoms ($X = \text{S, Se, Te}$) of the $1T$ -phase TMD $\text{Pt}X_2$ replaced by A atoms ($A = \text{Cd, Hg, Zn}$), and the monolayer is crystallized in $P\bar{3}m1$ space group (No. 164) with a buckled honeycomb lattice. The dynamically stable monolayer Pt_2HgSe_3 and its family materials Pt_2AX_3 ($A = \text{Hg, Cd, Zn}$; $X = \text{S, Se, Te}$) are \mathbb{Z}_2 topological insulators [48–55]. The monolayer ferromagnetic substrates, i.e. MY_2 ($M = \text{Fe, Co, Ni}$; $Y = \text{Cl, Br, I}$), ClI_3 , VI_3 , and MnBi_2Te_4 , are used to induce magnetic exchange interactions [56–71]. These two-dimensional magnets possess the ferromagnetic ground states in freestanding monolayer under the Curie temperatures as summarized in Table S2 [72]. By performing first-principles calculations, we systematically investigate the atomic, electronic, and topological properties of over 100 kinds of Pt_2AX_3 /ferromagnetic substrate van der Waals (vdW) heterostructures. By examining the lattice mismatch, stacking configuration, and band alignment, 44 kinds of well-matched vdW heterostructures are selected. Further analyses on band structures and topological properties demonstrate that these systems host valley polarization and exhibit different Berry curvature distributions at K/K' valleys.

In particular, we observe valley-polarized QAHE in $\text{Pt}_2\text{HgS}_3/\text{NiBr}_2$, $\text{Pt}_2\text{HgSe}_3/\text{CoBr}_2$, $\text{Pt}_2\text{HgSe}_3/\text{NiBr}_2$, and $\text{Pt}_2\text{ZnS}_3/\text{CoBr}_2$, with the Chern number of $\mathcal{C} = \pm 1$. We find a large valley splitting of 134.2 meV in $\text{Pt}_2\text{HgSe}_3/\text{NiBr}_2$ heterostructure and a considerable topological band gap of 58.8 meV in $\text{Pt}_2\text{HgS}_3/\text{NiBr}_2$ heterostructure. Both the monolayer jacutingaite family materials and the two-dimensional ferromagnetic substrates are energetically and dynamically stable [53, 56–60], greatly facilitating the experimental implementation of valley-polarized QAHE. Moreover, the structural stabilities of these Pt_2AX_3 -based vdW ferromagnetic het-

* Correspondence author: zhengliu@mail.ustc.edu.cn

† Correspondence author: han@fzu.edu.cn

‡ Correspondence author: qiao@ustc.edu.cn

erostuctures are also verified by molecular dynamic simulations [72].

II. CALCULATION METHODS

Our first-principles calculations were performed by using the projected augmented-wave method [73] as implemented in the Vienna *ab initio* simulation package (VASP) [74, 75]. The generalized gradient approximation of the Perdew-Burke-Ernzerhof (PBE) type was used to describe the exchange-correlation interaction [76]. The vdW interaction was treated by using DFT-D3 functional [77]. All atoms were fully relaxed until the Hellmann-Feynman force on each atom was less than 0.01 eV/Å. A vacuum buffer layer of 20 Å was used to avoid unnecessary interaction along z direction between adjacent slabs. The plane-wave energy cutoff was set to be 520 eV. The Γ -centered Monkhorst-Pack k -point grid of $11 \times 11 \times 1$ was adopted in all our calculations. To deal with the strong correlation effect of $3d$ magnetic elements (i.e., Fe, Co, Ni, Cr, V, and Mn), the GGA+ U method [78] was used with the corresponding on-site repulsion energy U and exchange interaction J [60–64] as described in Table S1 in supplemental materials [72]. Topological properties were calculated by using maximally-localized Wannier functions as implemented in Wannier90 and WannierTools software packages [79–81]. Spin-resolved band structures are extracted by using VASPKIT software [82] and PYPROCAR code [83]. Atomic structure and charge density difference are visualized by using VESTA software package [84].

III. ATOMIC STRUCTURES

Monolayer Pt_2AX_3 ($A = \text{Hg, Cd, Zn}$; $X = \text{S, Se, Te}$) is crystallized in $P\bar{3}m1$ space group (No. 164) with a buckled honeycomb structure as shown in Fig. 1(a). The A atoms are located at two different sublattices $A1$ and $A2$. The jacutingaite family monolayer Pt_2AX_3 belongs to Kane-Mele type topological insulator [52, 53], with the maximum band gap of 178 meV for Pt_2ZnSe_3 [53]. The typical band structures of monolayer Pt_2AX_3 are displayed in Figs. 1(b) and 1(c), where the Dirac points can be observed at K and K' valleys in the absence of SOC [see Fig. 1(b)]. When the SOC is considered, as shown in Fig. 1(c), a topological nontrivial band gap opens up around the two valleys. The valley degeneracy of monolayer Pt_2AX_3 is protected by the time-reversal symmetry and inversion symmetry, leading to $\Delta_K = \Delta_{K'}$.

In our calculations, we adopt 1×1 Pt_2AX_3 and different ferromagnetic substrates with suitable supercell to match the lattice constant. For example, the vdW heterostructure as shown in Fig. 1(a) consists of 1×1 Pt_2AX_3 and 2×2 MY_2 . To find the well-matched vdW heterostructures, we carry out the lattice mismatch calculations as plotted in Fig. 2 with orange stars and

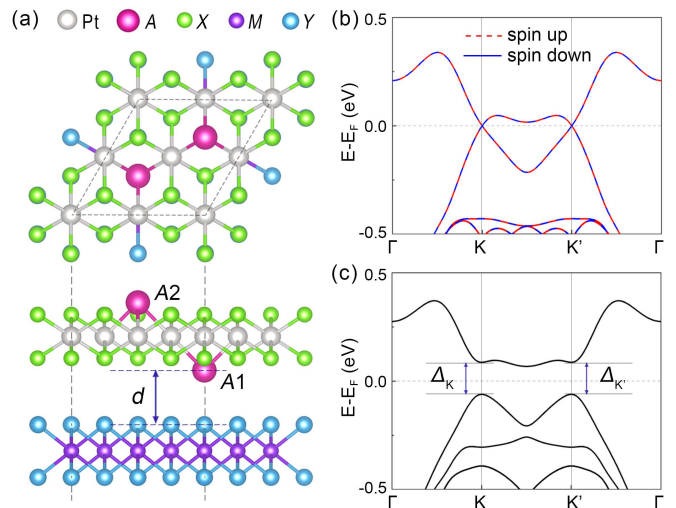


FIG. 1. (a) Top and side views of $\text{Pt}_2\text{AX}_3/\text{MY}_2$ heterostructure where 2×2 MY_2 is adopted to match 1×1 Pt_2AX_3 . d denotes the optimized vdW gap between the ferromagnetic substrate and jacutingaite family monolayer. $A1$ and $A2$ represent different sublattices of A atoms, where $A1$ locates closer to the ferromagnetic substrate. (b), (c) Band structures for the pristine jacutingaite Pt_2HgSe_3 monolayer (b) without and (c) with SOC. Δ_K and $\Delta_{K'}$ are local band gaps at valley K and K' valleys, respectively.

summarized in Table S3 in supplemental materials [72]. Considering the experimental feasibility, we mainly explore the physical properties of 62 kinds of heterostructures with lattice mismatch less than 5% as highlighted in Table S3 [72]. We then investigate the most stable stacking orders of these vdW heterostructures. For $\text{Pt}_2\text{AX}_3/\text{MY}_2$, we consider four stacking orders according to the atom site directly below $A1$ atoms: (i) M , (ii) Y (top), (iii) Y (hollow), and (iv) MY (bridge), respectively. Fig. 1(a) displays the type-i stacking configuration and the other three configurations are displayed in Fig. S3 in supplemental materials [72]. After geometrical optimization and total energy computation for different stacking orders, we summarize the most stable stacking configurations for every well-matched vdW heterostructure in Table S5 in supplemental materials [72].

IV. BAND ALIGNMENTS

To design functional devices based on heterostructures, band alignment is a crucial strategy that is widely used to analyze band edges of the two different materials forming a heterostructure [85, 86]. According to the different band gap positions, band alignment can be specified into three types: (I) straddling gap, (II) staggered gap, and (III) broken gap. Due to the type-III band alignment leading to the absence of global band gap in a heterostructure [87, 88], we apply the band alignment strategy to screen out the type-I and type-II vdW het-

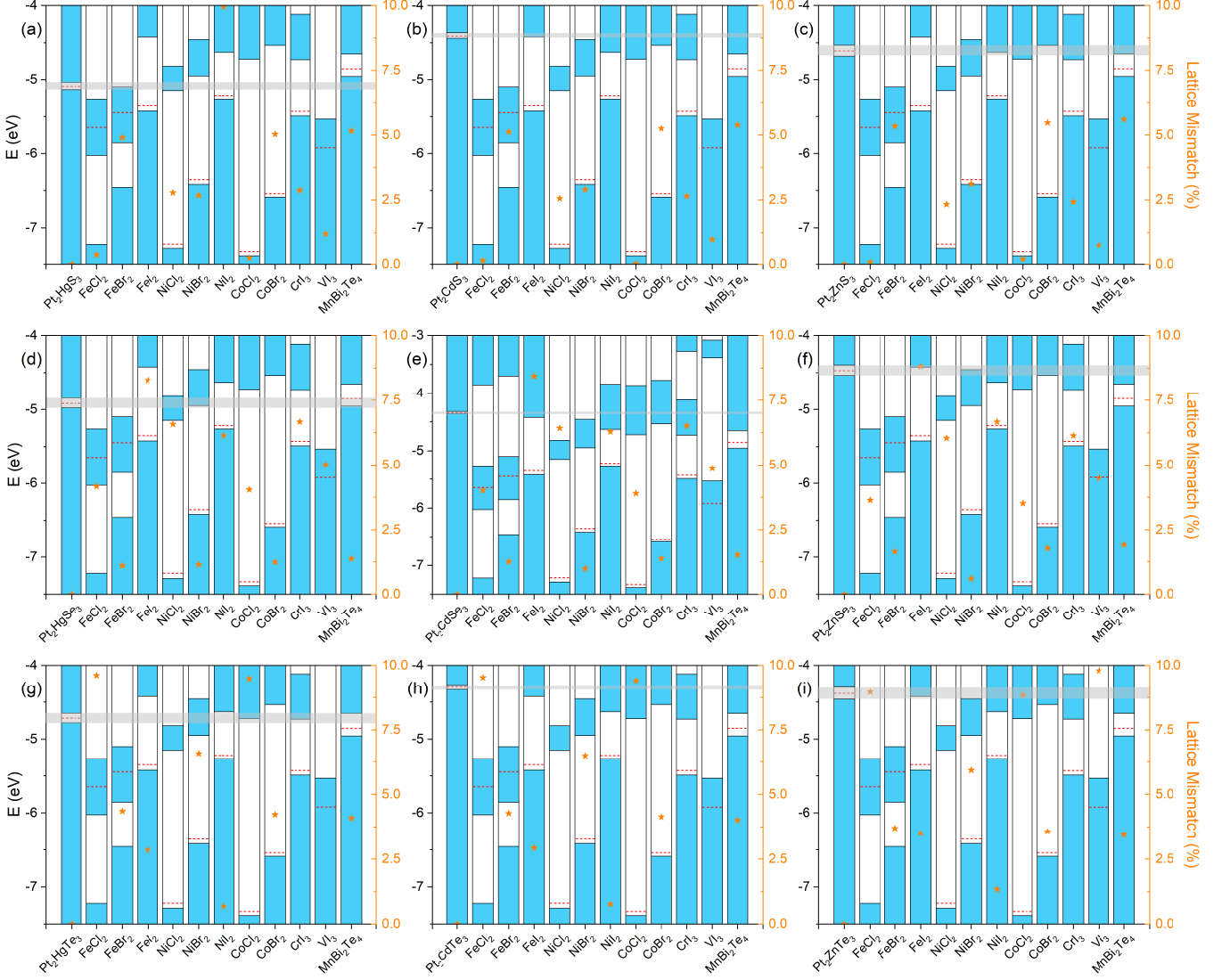


FIG. 2. Band alignments and lattice mismatch of jacutingaite family monolayer Pt_2AX_3 /ferromagnetic substrate heterostructures. Gray region stands for the intrinsic band gap of each jacutingaite family monolayer Pt_2AX_3 . The blue (white) area represents the presence (absence) of electronic states. Band edges are relative to the vacuum level by calculating work functions (dashed red line). Orange star (right axis) denotes the lattice mismatch of corresponding vdW heterostructure. (a)-(c), (d)-(f), and (g)-(i) represent the cases with $X = S, Se, Te$, respectively. (a)(d)(g), (b)(e)(h), and (c)(f)(i) represent the cases with $A = Hg, Cd, Zn$, respectively.

erostructures in order to obtain a global band gap.

Figure 2 displays the band alignments of jacutingaite family monolayer Pt_2AX_3 with different ferromagnetic substrates, which are obtained by calculating the work function and band structures of each freestanding material. We first take Pt_2HgS_3 as an example to analyze the band alignment. The first column in Fig. 2(a) represents the band edge of monolayer Pt_2HgS_3 , and the Fermi level (dashed red line) with respect to the vacuum level (0 eV) is about -5 eV lying inside the intrinsic band gap as displayed in gray region. The blue (white) area represents the presence (absence) of electronic states. One can find that the band gap of Pt_2HgS_3 layer lies in the

band gap of $NiBr_2$, resulting in a type-I heterostructure of $Pt_2HgS_3/NiBr_2$. Similarly, the $Pt_2HgS_3/FeBr_2$ system follows the type-II band alignment with the staggered gap. However, the $Pt_2HgS_3/NiCl_2$ system demonstrates the type-III nature because of the broken gap alignment, which will be excluded in our following discussions. By combing the band alignment and lattice mismatch analyses, we can filter out 44 kinds of vdW heterostructures from over 100 combinations as summarized in Table S5 in supplemental materials [72], in which we hopefully obtain global band gaps with Chern insulating phase after these heterostructures are formed.

TABLE I. Transferred charge ΔQ , vdW gap d , and magnetic moments of 8 kinds of typical $\text{Pt}_2\text{AX}_3/\text{MY}_2$ vdW heterostructures. ΔQ is extracted from the Bader charge analysis to evaluate the transferred electrons from the ferromagnetic substrate to Pt_2AX_3 layer. d represents the interlayer distance after full relaxation. M_{jac} , M_{tot} , M_{A1} , and M_{A2} denote the magnetic moment of Pt_2AX_3 layer, total vdW heterostructure, A1 atom, and A2 atom, respectively.

vdW Heterostructures	$\text{Pt}_2\text{HgS}_3/\text{CoBr}_2$	$\text{Pt}_2\text{HgSe}_3/\text{CoBr}_2$	$\text{Pt}_2\text{HgTe}_3/\text{CoBr}_2$	$\text{Pt}_2\text{ZnS}_3/\text{CoBr}_2$	$\text{Pt}_2\text{HgS}_3/\text{NiBr}_2$	$\text{Pt}_2\text{HgSe}_3/\text{NiBr}_2$	$\text{Pt}_2\text{CdS}_3/\text{NiBr}_2$	$\text{Pt}_2\text{ZnSe}_3/\text{NiBr}_2$
ΔQ (e)	-0.17	-0.20	-0.09	-0.32	-0.03	-0.11	-0.18	-0.17
d (\AA)	2.51	2.74	2.90	2.70	2.28	2.46	2.18	2.51
M_{jac} (μ_B)	0.330	0.061	0.068	0.050	0.219	0.204	0.276	0.167
M_{tot} (μ_B)	11.525	11.530	11.490	11.503	7.453	7.446	7.392	7.420
M_{A1} (μ_B)	0.005	-0.009	-0.005	-0.014	-0.016	-0.021	-0.020	0.009
M_{A2} (μ_B)	0.056	0.016	0.007	0.024	0.067	0.045	0.104	0.027

V. INTERFACIAL ELECTRONIC AND MAGNETIC PROPERTIES

When two different materials form heterostructures, the charge transfer process usually exists and further modifies the electronic and magnetic properties of the heterostructure [89–91]. To explore the interfacial electronic properties of the Pt_2AX_3 /ferromagnetic insulator vdW heterostructures, we calculate the charge density difference and the planar-averaged electrostatic potential along z direction. Here, we take eight typical systems with CoBr_2 and NiBr_2 substrates to illustrate the charge transfer process as shown in Fig. 3, Table I and Figs. S10-S11 in supplemental materials [72].

For $\text{Pt}_2\text{HgSe}_3/\text{NiBr}_2$, as displayed in Fig. 3(a), the planar-averaged electrostatic potential along z direction in Pt_2HgSe_3 layer is no longer symmetric with respect to the Pt atomic layer, indicating the presence of charge transfer process at the interface. More quantitatively, the Bader charge analysis demonstrates the transferred charge ΔQ from NiBr_2 layer to Pt_2HgSe_3 layer is $-0.11e$. The charge density difference, as illustrated in Fig. 3(b), also demonstrates that the NiBr_2 layer accumulates electrons whereas the Pt_2HgSe_3 layer loses electrons after they form a heterostructure. As a result, a built-in electric field ΔV_z appears at the interface as displayed in Fig. 3(a), which can further enhance the Rashba SOC of the $\text{Pt}_2\text{HgSe}_3/\text{NiBr}_2$ system.

Table I displays the transferred charge ΔQ , vdW gap d , and magnetic moments of the eight typical $\text{Pt}_2\text{AX}_3/\text{MY}_2$ vdW heterostructures. One can observe that all the interlayer vdW gaps d become smaller than the initial state after full structural relaxation. Due to the smaller atomic radius of S atom compared to Se atom, Pt_2HgS_3 tends to move closer to the substrate than Pt_2HgSe_3 when constructing a heterostructure with the same substrate. Moreover, d in $\text{Pt}_2\text{AX}_3/\text{NiBr}_2$ is generally smaller than that in $\text{Pt}_2\text{AX}_3/\text{CoBr}_2$. The shorter d in $\text{Pt}_2\text{AX}_3/\text{NiBr}_2$ leads to a stronger magnetic proximity effect and large magnetization M_{jac} in jacutingaite layer. The magnetic proximity effect also induces different magnetic moments M_{A1} and M_{A2} on A1 and A2 because of the different distances to the substrate. The presence of a the ferromag-

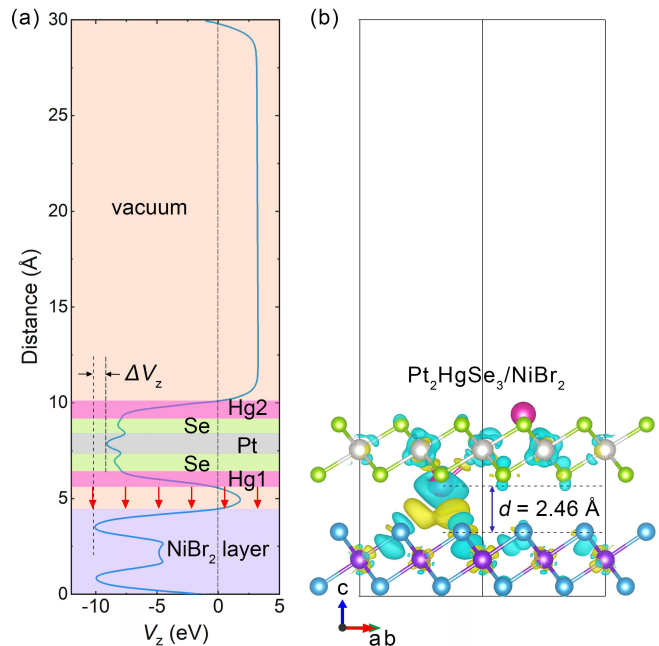


FIG. 3. (a) The planar-averaged electrostatic potential V_z and (b) charge density difference of the $\text{Pt}_2\text{HgSe}_3/\text{NiBr}_2$ heterostructure. V_z in Pt_2HgSe_3 layer is asymmetric with respect to the Pt atomic layer, indicating the charge transfer at the interface. Highlighted regions in (a) correspond to associated horizontal atomic layers in (b). Cyan and yellow contours represent charge depletion and accumulation, respectively.

netic substrate breaks both inversion and time-reversal symmetries and leads to inequivalent exchange fields on A1 and A2 atoms, which lifts the spin degeneracy and valley-dependent band gaps. Nonzero Berry curvature and anomalous Hall responses can also appear [38]. For example, in $\text{Pt}_2\text{HgSe}_3/\text{NiBr}_2$, the magnetic moment of Hg2 atom is $0.045 \mu_B$ and is parallel to that of NiBr_2 , whereas an antiparallel magnetic moment of $-0.021 \mu_B$ is induced in Hg1 atom. Consequently, the valley degeneracy of Pt_2AX_3 can be lifted by the proximity effect induced broken time-reversal symmetry and Rashba SOC. Hereinbelow, we explore the electronic properties of these

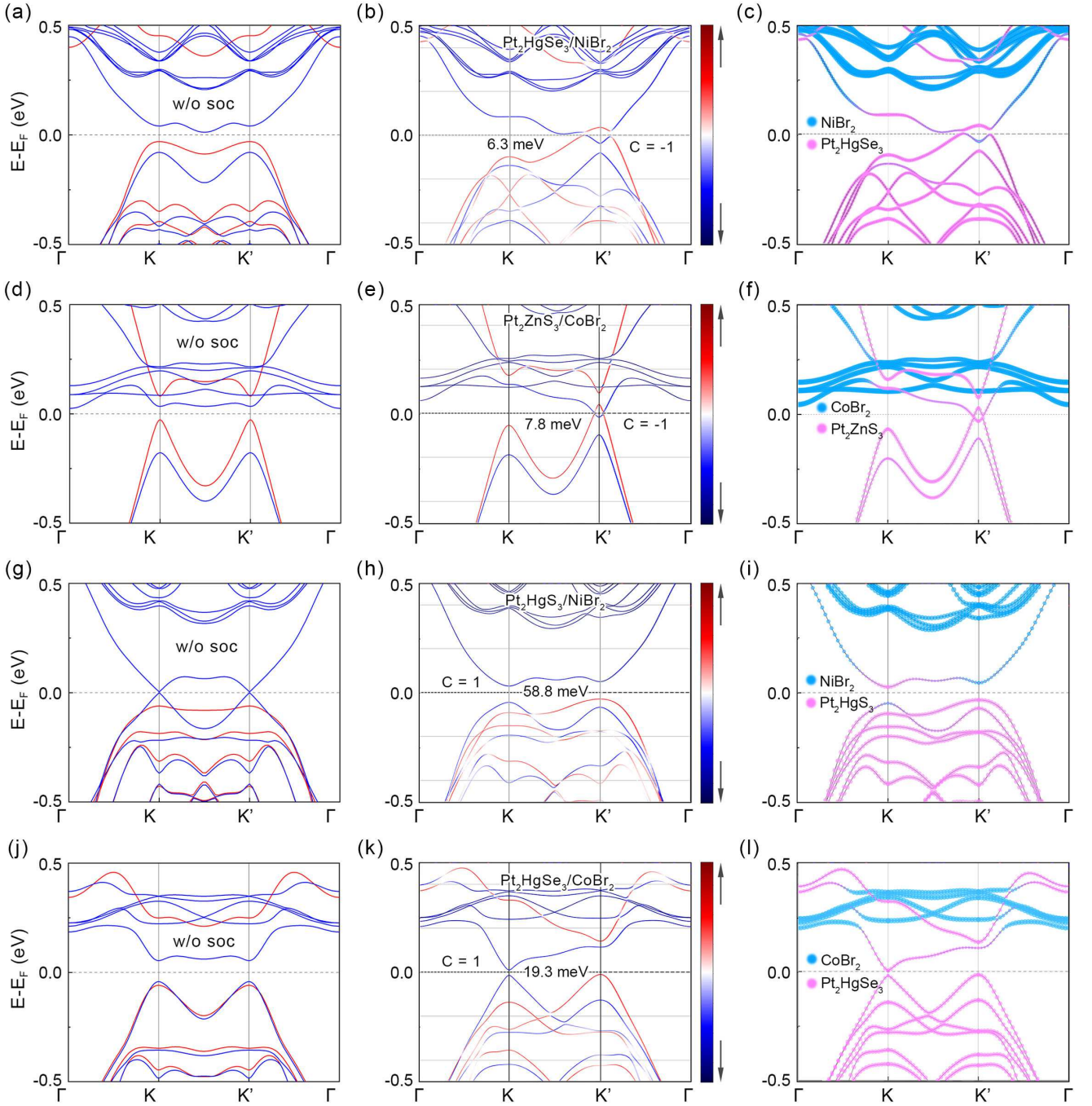


FIG. 4. (a)-(b) Spin-resolved band structures of the $\text{Pt}_2\text{HgSe}_3/\text{NiBr}_2$ heterostructure (a) without and (b) with SOC, respectively. (d)-(e) Spin-resolved band structures of the $\text{Pt}_2\text{ZnS}_3/\text{CoBr}_2$ heterostructure (d) without and (e) with SOC, respectively. (g)-(h) Spin-resolved band structures of the $\text{Pt}_2\text{HgS}_3/\text{NiBr}_2$ heterostructure (g) without and (h) with SOC, respectively. (j)-(k) Spin-resolved band structures of the $\text{Pt}_2\text{HgSe}_3/\text{CoBr}_2$ heterostructure (j) without and (k) with SOC, respectively. The red (blue) color denotes the spin-up (spin-down) state. The Chern number C and the global band gap for every system is demonstrated in (b), (e), (h), and (k), respectively. (c), (f), (i), (l) Layer-resolved band structures of (c) $\text{Pt}_2\text{HgSe}_3/\text{NiBr}_2$, (f) $\text{Pt}_2\text{ZnS}_3/\text{CoBr}_2$, (i) $\text{Pt}_2\text{HgS}_3/\text{NiBr}_2$, and (l) $\text{Pt}_2\text{HgSe}_3/\text{CoBr}_2$. The pink bubble represents the element projection of jacutingaite family layer whereas the light blue bubble represents the element projection of ferromagnetic substrate layer.

Pt₂AX₃/ferromagnetic substrate vdW heterostructures.

VI. ELECTRONIC AND TOPOLOGICAL PROPERTIES

After calculating band structures and topological properties of the 44 kinds of well-matched Pt₂AX₃/ferromagnetic substrate vdW heterostructures, we find four systems are topologically nontrivial, whereas the remaining systems are topologically trivial (see Figs. S12-S22 in supplemental materials [72] for band structures of all 44 systems). Figure 4 shows the spin-resolved and layer-resolved band structures of the four topologically nontrivial systems, i.e., Pt₂HgSe₃/NiBr₂, Pt₂ZnS₃/CoBr₂, Pt₂HgS₃/NiBr₂, and Pt₂HgSe₃/CoBr₂.

We start from Pt₂HgSe₃/NiBr₂ as an example [see Figs. 4(a)-4(c)]. In the absence of SOC, as shown in Fig. 4(a), we can observe that the magnetic proximity effect of ferromagnetic substrates induces sizable Zeeman splitting but keeps the valley degeneracy. Further calculations on the band structures with and without magnetization also demonstrate that the band structures of the Pt₂AX₃ near the Fermi level are modified by the magnetic exchange interaction [72]. When SOC is considered, as displayed in Fig. 4(b), a band inversion appears around K' point with a band gap of 6.3 meV induced by Rashba SOC, whereas the bands close to the Fermi level around K point move far away from each other in a repulsive manner, forming a sizable local band gap of Δ_K of 182.8 meV. The difference around K/K' valleys results in a large valley splitting of 134.2 meV. We can also observe from the layer-resolved band structures as shown in Fig. 4(c) that the electronic states near the Fermi level are mainly dominated by the topological Pt₂HgSe₃ layer, indicating the electronic structures of the Pt₂HgSe₃ monolayer are modified after coupled to the NiBr₂ substrate.

The above band analysis can be applied to the remaining three nontrivial systems. For Pt₂ZnS₃/CoBr₂ system, as shown in Figs. 4(d)-4(f), the band structures are similar to that of Pt₂HgSe₃/NiBr₂ with a band inversion and a global band gap of 7.8 meV around K' point induced by Rashba SOC. For Pt₂HgS₃/NiBr₂ and Pt₂HgSe₃/CoBr₂ systems, as illustrated in Figs. 4(g)-4(l), the bands are different from that of Pt₂HgSe₃/NiBr₂, where the local gap at K valley is smaller than that at K' valley. Table II summarizes the extracted valley splitting Δ , global band gaps E_g , local band gaps $\Delta_K/\Delta_{K'}$ at valleys K/K' , and Chern numbers \mathcal{C} for above four vdW heterostructures. One can see that the valley polarization generally exists in these systems (also see Table S5 in supplemental materials [72] for the remaining 40 kinds of heterostructures). Among the 44 systems, the Pt₂HgSe₃/NiBr₂ exhibits the maximum valley splitting of 134.2 meV, which is an order of magnitude larger than experimental observations in TMD/ferromagnetic substrate systems [92, 93], provid-

TABLE II. Valley splitting Δ , global band gap E_g , local band gaps $\Delta_K/\Delta_{K'}$ at K/K' valleys, and Chern number \mathcal{C} for nontrivial jacutingaite family monolayer/ferromagnetic substrate vdW heterostructures. Valley splitting is evaluated via the difference between the valence band maximum at valley K/K' , i.e. $\Delta = E_V(K') - E_V(K)$.

Nontrivial vdW Heterostructures	Δ (meV)	E_g (meV)	Δ_K (meV)	$\Delta_{K'}$ (meV)	\mathcal{C}
Pt ₂ HgSe ₃ /NiBr ₂	134.2	6.3	182.8	73.5	-1
Pt ₂ ZnS ₃ /CoBr ₂	36.3	7.8	185.9	59.9	-1
Pt ₂ HgS ₃ /NiBr ₂	15.4	58.8	74.2	78.8	1
Pt ₂ HgSe ₃ /CoBr ₂	3.5	19.3	22.8	124.0	1

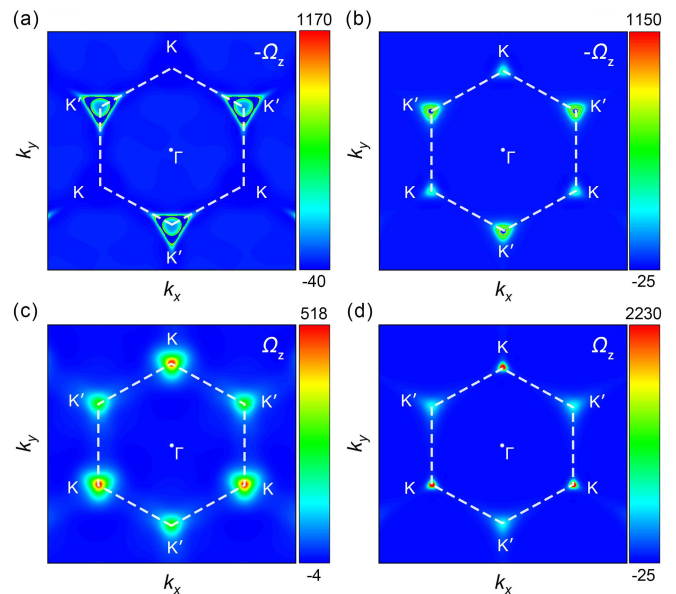


FIG. 5. Berry curvature distributions in the first Brillouin zone of four nontrivial vdW heterostructures (a) Pt₂HgSe₃/NiBr₂, (b) Pt₂ZnS₃/CoBr₂, (c) Pt₂HgS₃/NiBr₂, and (d) Pt₂HgSe₃/CoBr₂, respectively. Berry curvature is centered around the K/K' valleys and is absent elsewhere but dissimilarly distributes in the two inequivalent valleys K/K' . For clarity, (a) and (b) plot $-\Omega_z$ whereas (c) and (d) plot Ω_z .

ing an ideal platform to realize topological valleytronics.

To evaluate the topology of the above band structures, we compute the Berry curvature of all occupied bands in each system by using maximally localized Wannier functions [79, 80]. We carry out orbital projections for every insulating system to guide the Wannier functions. For example, by analyzing the orbital projection on each kind of elements Pt₂HgSe₃/NiBr₂, we find that Pt- d , Hg- s , Se- p , Ni- d , and Br- p orbitals are distributed around Fermi level (see Figs. S1-S2 in supplemental materials [72]). Figure 5 displays the Berry curvature distributions of above four systems in the first Brillouin zone. One can see that the Berry curvature is centered around the K/K' valleys but is absent elsewhere. The value

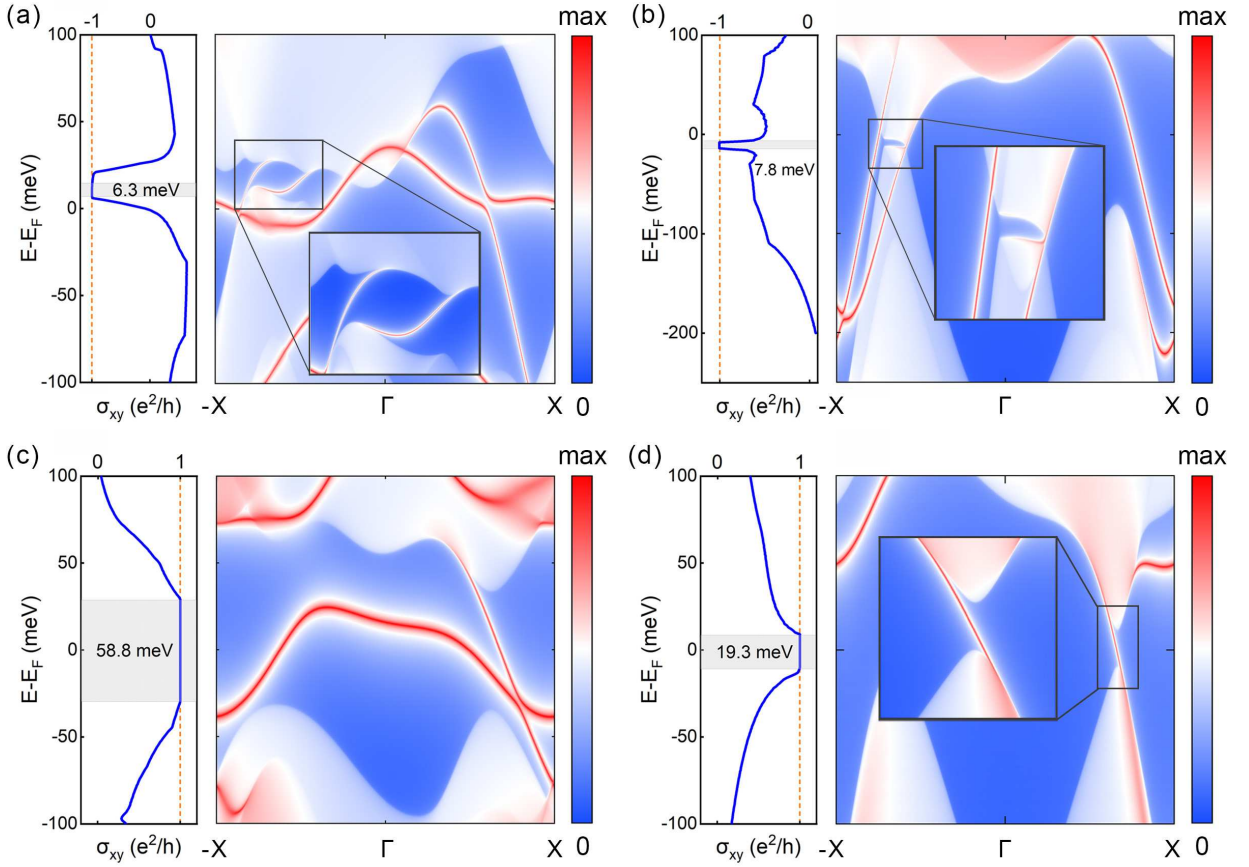


FIG. 6. Anomalous Hall conductivity σ_{xy} and local density of states (LDOS) of four nontrivial vdW heterostructures (a) $\text{Pt}_2\text{HgSe}_3/\text{NiBr}_2$, (b) $\text{Pt}_2\text{ZnS}_3/\text{CoBr}_2$, (c) $\text{Pt}_2\text{HgS}_3/\text{NiBr}_2$, and (d) $\text{Pt}_2\text{HgSe}_3/\text{CoBr}_2$. Insets correspond to enlarged views of edge states. In all LDOS plots, there are chiral edge states connecting conduction bands and valence bands.

of the Berry curvature around K/K' valleys depends on the specific material combinations, i.e., the Berry curvature only appears in K' valley for $\text{Pt}_2\text{HgSe}_3/\text{NiBr}_2$ as displayed in Fig. 5(a), while it exists in both K and K' valleys with different magnitudes for other three systems as shown in Figs. 5(b)-5(d). By integrating the Berry curvature all over the first Brillouin zone, we can obtain the Chern numbers as listed in Table II. The nonzero Chern number indicates the nontrivial band topology in the four systems, i.e., the formation of QAHE. Combining the valley polarizations and different Berry curvature distributions at the two inequivalent valleys, we can find that these four systems can implement valley-polarized QAHE. More strikingly, the global band gap of 58.8 meV in $\text{Pt}_2\text{HgS}_3/\text{NiBr}_2$ is over three times larger than that in $\text{Pt}_2\text{HgSe}_3/\text{CrI}_3$ heterostructure (17.2 meV) as predicted in our previous report [38], implying the potential for high-temperature QAHE [94–99]. Surprisingly, the magnetocrystalline anisotropy energy (MAE) calculation shows that the MAE of $\text{Pt}_2\text{ZnS}_3/\text{CoBr}_2$ heterostructure is 1.795 meV/Co, suggesting the magnetic easy axis of CoBr_2 can be tuned by Pt_2ZnS_3 to out-of-plane direction [72], which is beneficial to the experimental realization of valley-polarized QAHE.

The nontrivial topology of the four systems can also be confirmed by the anomalous Hall conductivity σ_{xy} and the local density of states (LDOS) calculations, as displayed in Fig. 6. The anomalous Hall conductivity in Figs. 6(a) and 6(b) demonstrates a quantized Hall plateau of $\sigma_{xy} = -e^2/h$ in $\text{Pt}_2\text{HgSe}_3/\text{NiBr}_2$ and $\text{Pt}_2\text{ZnS}_3/\text{CoBr}_2$ systems when the Fermi energy lies inside the global band gap, which is a strong evidence for QAHE. Similarly, in Figs. 6(c) and 6(d), we can also observe that the anomalous Hall conductivity is quantized as $\sigma_{xy} = e^2/h$ in $\text{Pt}_2\text{HgS}_3/\text{NiBr}_2$ and $\text{Pt}_2\text{HgSe}_3/\text{CoBr}_2$ systems. Such a Chern insulating topological phase is also confirmed by the LDOS of these nontrivial systems since there are chiral edge states in the global band gaps connecting conduction bands and valence bands.

VII. SUMMARY AND CONCLUSION

In this work, we proposed an excellent platform to implement valley polarization and valley-polarized QAHE based on the vdW heterostructure constructed by monolayer jacutingaite family materials Pt_2AX_3 and two-dimensional ferromagnetic substrates. We systematically

investigated atomic structures, band alignments, interfacial characteristics, electronic and topological properties of over 100 kinds of Pt_2AX_3 /ferromagnetic substrate heterostructures. By using the band alignment strategy, we filtered out 44 kinds of well-matched systems with potential for global band gaps. We evaluated the interfacial characteristics by analyzing the charge density difference, Bader charge transferring, planar-averaged electrostatic potential, and magnetic properties. The interlayer charge transfer leads to a built-in electric field and the asymmetric atomic structure results in a broken inversion symmetry. Furthermore, the reducing interlayer vdW gap leads to a strong magnetic proximity, which induces large magnetization in Kane-Mele type topological insulator Pt_2AX_3 . Consequently, the valley degeneracy is lifted by the breaking of time-reversal symmetry and inversion symmetry. We found the general valley polarization in the 44 kinds of well-matched systems and observed a sizable valley splitting of 134.2 meV in $\text{Pt}_2\text{HgSe}_3/\text{NiBr}_2$ system.

Particularly, we identified four Chern insulators in $\text{Pt}_2\text{HgS}_3/\text{NiBr}_2$, $\text{Pt}_2\text{HgSe}_3/\text{CoBr}_2$, $\text{Pt}_2\text{HgSe}_3/\text{NiBr}_2$, and $\text{Pt}_2\text{ZnS}_3/\text{CoBr}_2$ due to their nontrivial band topology. In addition to the valley polarization, we also observed different Berry curvature distributions in the two inequivalent valleys K/K' in these four systems, indicating the presence of valley-polarized QAHE. Eventually, we obtained valley-polarized QAHE with total Chern numbers $\mathcal{C} = \pm 1$ in the vdW heterostructures based on

monolayer jacutingaite family materials. Most surprisingly, we observed a sizable nontrivial global band gap of 58.8 meV in the $\text{Pt}_2\text{HgS}_3/\text{NiBr}_2$ system with potential implementation for the high-temperature QAHE.

In conclusion, valley polarization universally exists in the ferromagnetic vdW heterostructures based on monolayer jacutingaite family materials and several valley-polarized QAHE vdW heterostructures can be achieved when the valley splitting is strong enough to lead to a band inversion. Our work proposes an excellent platform based on monolayer jacutingaite family materials Pt_2AX_3 to implement topological valleytronics and may stimulate more applications on the two-dimensional valley-polarized topological systems.

ACKNOWLEDGMENTS

We are grateful to Prof. Yang Gao for helpful advice and discussions. This work was financially supported by the National Natural Science Foundation of China (No. 11974327 and No. 12004369), Fundamental Research Funds for the Central Universities (WK3510000010, WK2030020032), Anhui Initiative in Quantum Information Technologies (Grant No. AHY170000). We also thank for the high-performance supercomputing services provided by AM-HPC and the Supercomputing Center of University of Science and Technology of China.

-
- [1] A. K. Geim and K. S. Novoselov, *Nat. Mater.* **6**, 183 (2007).
- [2] K. Wang, T. Hou, Y. Ren, and Z. Qiao, *Front. Phys.* **14**, 23501 (2019).
- [3] J. Zeng, R. Xue, T. Hou, Y. Han, and Z. Qiao, *Front. Phys.* **17**, 63503 (2022).
- [4] H. Yang, J. Zeng, S. You, Y. Han, and Z. Qiao, *Front. Phys.* **17**, 63508 (2022).
- [5] Q. H. Wang, K. Kalantar-Zadeh, A. Kis, J. N. Coleman, and M. S. Strano, *Nat. Nanotechnol.* **7**, 699 (2012).
- [6] G. Luo, Z.-Z. Zhang, H.-O. Li, X.-X. Song, G.-W. Deng, G. Cao, M. Xiao, and G.-P. Guo, *Front. Phys.* **12**, 128502 (2017).
- [7] M. Cheng, J. Yang, X. Li, H. Li, R. Du, J. Shi, and J. He, *Front. Phys.* **17**, 63601 (2022).
- [8] D. J. Ibberson, L. Bourdet, J. C. Abadillo-Uriel, I. Ahmed, S. Barraud, M. J. Caldern, Y.-M. Niquet, and M. F. GonzalezZalba, *Appl. Phys. Lett.* **113**, 053104 (2018).
- [9] M. Tahir, A. Manchon, K. Sabeeh, and U. Schwingenschlgl, *Appl. Phys. Lett.* **102**, 162412 (2013).
- [10] C. J. Tabert and E. J. Nicol, *Phys. Rev. B* **87**, 235426 (2013).
- [11] Y. Li, J. Ludwig, T. Low, A. Chernikov, X. Cui, G. Arefe, Y. D. Kim, A. M. van der Zande, A. Rigosi, H. M. Hill, S. H. Kim, J. Hone, Z. Li, D. Smirnov, and T. F. Heinz, *Phys. Rev. Lett.* **113**, 266804 (2014).
- [12] C. Zhao, T. Norden, P. Zhang, P. Zhao, Y. Cheng, F. Sun, J. P. Parry, P. Taheri, J. Wang, Y. Yang, T. Scrase, K. Kang, S. Yang, G.-X. Miao, R. Sabirianov, G. Kiioseoglou, W. Huang, A. Petrou, and H. Zeng, *Nat. Nanotechnol.* **12**, 757 (2017).
- [13] Si-Yu Li, Ying Su, Ya-Ning Ren, and Lin He, *Phys. Rev. Lett.* **124**, 106802 (2020).
- [14] W. Yao, D. Xiao, and Q. Niu, *Phys. Rev. B* **77**, 235406 (2008).
- [15] K. L. Seyler, D. Zhong, B. Huang, X. Linpeng, N. P. Wilson, T. Taniguchi, K. Watanabe, W. Yao, D. Xiao, M. A. McGuire, K.-M. C. Fu, and X. Xu, *Nano Lett.* **18**, 3823 (2018).
- [16] M. S. Mrudul, . Jimnez-Galn, M. Ivanov, and G. Dixit, *Optica* **8**, 422 (2021).
- [17] J. R. Schaibley, H. Yu, G. Clark, P. Rivera, J. S. Ross, K. L. Seyler, W. Yao, and X. Xu, *Nat. Rev. Mat.* **1**, 16055 (2016).
- [18] D. Xiao, G.-B. Liu, W. Feng, X. Xu, and W. Yao, *Phys. Rev. Lett.* **108**, 196802 (2012).
- [19] K. Behnia, *Nat. Nanotechnol.* **7**, 488 (2012).
- [20] S. A. Wolf, D. D. Awschalom, R. A. Buhrman, J. M. Daughton, S. Von Molnr, M. L. Roukes, A. Y. Chtchelkanova, and D. M. Treger, *Science* **294**, 1488 (2001).
- [21] A. Rycerz, J. Tworzydo, and C. Beenakker, *Nat. Phys.* **3**, 172 (2007).
- [22] D. Pesin and A. H. MacDonald, *Nat. Mater.* **11**, 409 (2012).
- [23] P. San-Jose, E. Prada, E. McCann, and H. Schomerus, *Phys. Rev. Lett.* **102**, 247204 (2009).

- [24] Y. S. Ang, S. A. Yang, C. Zhang, Z. Ma, and L. K. Ang, *Phys. Rev. B* **96**, 245410 (2017).
- [25] J. Li, R.-X. Zhang, Z. Yin, J. Zhang, K. Watanabe, T. Taniguchi, C. Liu, and J. Zhu, *Science* **362**, 1149 (2018).
- [26] F. D. M. Haldane, *Phys. Rev. Lett.* **61**, 2015 (1988).
- [27] Y. Ren, Z. Qiao, and Q. Niu, *Rep. Prog. Phys.* **79**, 066501 (2016).
- [28] C.-Z. Chang, J. Zhang, X. Feng, J. Shen, Z. Zhang, M. Guo, K. Li, Y. Ou, P. Wei, L. Wang, Z. Ji, Y. Feng, S. Ji, X. Chen, J. Jia, X. Dai, Z. Fang, S.-C. Zhang, K. He, and Y. Wang, L. Lu, X.-C. Ma, Q.-K. Xue, *Science* **340**, 167 (2013).
- [29] Y. Deng, Y. Yu, M. Z. Shi, J. Wang, X. H. Chen, and Y. Zhang, *Science* **367**, 895 (2020).
- [30] Z. Qiao, S. A. Yang, W. Feng, W.-K. Tse, J. Ding, Y. Yao, J. Wang, and Q. Niu, *Phys. Rev. B* **82**, 161414 (2010).
- [31] Z. Qiao, W. Ren, H. Chen, L. Bellaiche, Z. Zhang, A. H. MacDonald, and Q. Niu, *Phys. Rev. Lett.* **112**, 116404 (2014).
- [32] R. Yu, W. Zhang, H.-J. Zhang, S.-C. Zhang, X. Dai, and Z. Fang, *Science* **329**, 61 (2010).
- [33] J. Zhang, B. Zhao, T. Zhou, Y. Xue, C. Ma, and Z. Yang, *Phys. Rev. B* **97**, 085401 (2018).
- [34] J. Kim, X. Hong, C. Jin, S.-F. Shi, C.-Y. S. Chang, M.-H. Chiu, L.-J. Li, and F. Wang, *Science* **346**, 1205 (2014).
- [35] A. Srivastava, M. Sidler, A. V. Allain, D. S. Lembke, A. Kis, and A. Imamoglu, *Nat. Phys.* **11**, 141 (2015).
- [36] H. Rostami and R. Asgari, *Phys. Rev. B* **91**, 075433 (2015).
- [37] Y. Li, J. Ludwig, T. Low, A. Chernikov, X. Cui, G. Arefe, Y. D. Kim, A. M. van der Zande, A. Rigosi, H. M. Hill, S. H. Kim, J. Hone, Z. Li, D. Smirnov, and T. F. Heinz, *Phys. Rev. Lett.* **113**, 266804 (2014).
- [38] Z. Liu, Y. Han, Y. Ren, Q. Niu, and Z. Qiao, *Phys. Rev. B* **104**, L121403 (2021).
- [39] M. Bora, S. K. Behera, P. Samal, and P. Deb, *Phys. Rev. B* **105**, 235422 (2022).
- [40] H. Zhang, W. Yang, Y. Ning, and X. Xu, *Phys. Rev. B* **101**, 205404 (2020).
- [41] Marc Vila, Jose H. Garcia, and Stephan Roche, *Phys. Rev. B* **104**, L161113 (2021).
- [42] M. Ur Rehman, Z. Qiao, and Jian Wang, *Phys. Rev. B* **105**, 165417 (2022).
- [43] M. Ur Rehman, M. Kiani, and Jian Wang, *Phys. Rev. B* **105**, 195439 (2022).
- [44] H. Pan, Z. Li, C.-C. Liu, G. Zhu, Z. Qiao, and Y. Yao, *Phys. Rev. Lett.* **112**, 106802 (2014).
- [45] J. Zhou, Q. Sun, and P. Jena, *Phys. Rev. Lett.* **119**, 046403 (2017).
- [46] Z. Liu, Y. Ren, Y. Han, Q. Niu, Z. Qiao, *arXiv:2202.00221*.
- [47] F. Zhan, Z. Ning, L.-Y. Gan, B. g Zheng, J. Fan, and R. Wang, *Phys. Rev. B* **105**, L081115 (2022).
- [48] I. Cucchi, A. Marrazzo, E. Cappelli, S. Ricco, F. Y. Bruno, S. Lisi, M. Hoesch, T. K. Kim, C. Cacho, C. Besnard, E. Giannini, N. Marzari, M. Gibertini, F. Baumberger, and A. Tamai, *Phys. Rev. Lett.* **124**, 106402 (2020).
- [49] K. Kandrai, P. Vancso, G. Kukucska, J. Koltai, G. Baranka, A. Hoffmann, A. Pekker, K. Kamaras, Z. E. Horvath, A. Vymazalova, L. Tapasztó, and P. Nemes-Incze, *Nano Lett.* **20**, 5207 (2020).
- [50] A. Marrazzo, M. Gibertini, D. Campi, N. Mounet, and N. Marzari, *Phys. Rev. Lett.* **120**, 117701 (2018).
- [51] A. Marrazzo, M. Gibertini, D. Campi, N. Mounet, and N. Marzari, *Nano Lett.* **19**, 8431 (2019).
- [52] C. L. Kane and E. J. Mele, *Phys. Rev. Lett.* **95**, 146802 (2005).
- [53] F. Crasto de Lima, R. H. Miwa, and A. Fazzio, *Phys. Rev. B* **102**, 235153 (2020).
- [54] C. Ma, H. Forster, and G. Grundmann, *Crystals* **10**, 687 (2020).
- [55] A. Marrazzo, N. Marzari, and M. Gibertini, *Phys. Rev. Res.* **2**, 012063 (2020).
- [56] M. A. McGuire, *Crystals* **7**, 121 (2017).
- [57] V. V. Kulish and W. Huang, *J. Mater. Chem. C* **5**, 8734 (2017).
- [58] B. Huang, G. Clark, E. N.-Moratalla, D. R. Klein, R. Cheng, K. L. Seyler, D. Zhong, E. Schmidgall, M. A. McGuire, D. H. Cobden, W. Yao, Di Xiao, P. J.-Herrero and X. Xu, *Nature (London)* **546**, 270 (2017).
- [59] M.M. Otrokov, I.P. Rusinov, M. Blanco-Rey, M. Hoffmann, A.Yu. Vyazovskaya, S.V. Ereemeev, A. Ernst, P.M. Echenique, A. Arnau, and E.V. Chulkov, *Phys. Rev. Lett.* **122**, 107202 (2019).
- [60] S. Tian, J.-F. Zhang, C. Li, T. Ying, S. Li, X. Zhang, K. Liu, and H. Lei, *J. Am. Chem. Soc.* **141**, 5326 (2019).
- [61] H. Y. Lv, W. J. Lu, X. Luo, X. B. Zhu, and Y. P. Sun, *Phys. Rev. B* **99**, 134416 (2019).
- [62] A. S. Botana, and M. R. Norman, *Phys. Rev. Mater.* **3**, 044001 (2019).
- [63] M. M. Otrokov, I. P. Rusinov, M. Blanco-Rey, M. Hoffmann, A. Yu. Vyazovskaya, S. V. Ereemeev, A. Ernst, P. M. Echenique, A. Arnau, and E. V. Chulkov, *Phys. Rev. Lett.* **122**, 107202 (2019).
- [64] X. Li, Z. Zhang, and H. Zhang, *Nanoscale Adv.* **2**, 495 (2020).
- [65] M. Lu, Q. Yao, C. Xiao, C. Huang, and E. Kan, *ACS Omega* **4**, 5714 (2019).
- [66] D. Zhong, K. L. Seyler, X. Linpeng, R. Cheng, N. Sivadas, B. Huang, E. Schmidgall, T. Taniguchi, K. Watanabe, M. A. McGuire, W. Yao, D. Xiao, K.-M. C. Fu, and X. Xu, *Sci. Adv.* **3**, e1603113 (2017).
- [67] L. Webster and J.-A. Yan, *Phys. Rev. B* **98**, 144411 (2018).
- [68] C. Gong, L. Li, Z. Li, H. Ji, A. Stern, Y. Xia, T. Cao, W. Bao, C. Wang, Y. Wang, Z. Q. Qiu, R. J. Cava, S. G. Louie, J. Xia, and X. Zhang, *Nature (London)* **546**, 265 (2017).
- [69] S. Jiang, J. Shan, and K. F. Mak, *Nat. Mater.* **17**, 406 (2018).
- [70] K. F. Mak, J. Shan, and D. C. Ralph, *Nat. Rev. Phys.* **1**, 646 (2019).
- [71] W. Zhuo, B. Lei, S. Wu, F. Yu, C. Zhu, J. Cui, Z. Sun, D. Ma, M. Shi, H. Wang, W. Wang, T. Wu, J. Ying, S. Wu, Z. Wang, and X. Chen, *Adv. Mater.* **33**, 2008586 (2021).
- [72] See Supplemental Materials at [XXXURL] for more information about calculation details, ferromagnetic substrates, vdW heterostructure configurations, orbital projections, molecular dynamic simulations, more band structures, manipulated band gaps, charge density differences and the planar-averaged electrostatic potentials of other well-matched systems.
- [73] P. E. Blöchl, *Phys. Rev. B* **50**, 17953 (1994).
- [74] G. Kresse and J. Furthmüller, *Phys. Rev. B* **54**, 11169 (1996).

- [75] G. Kresse and D. Joubert, *Phys. Rev. B* **59**, 1758 (1999).
- [76] J. P. Perdew, J. A. Chevary, S. H. Vosko, K. A. Jackson, M. R. Pederson, D. J. Singh, and C. Fiolhais, *Phys. Rev. B* **46**, 6671 (1992).
- [77] S. Grimme, J. Antony, S. Ehrlich, and H. Krieg, *J. Chem. Phys.* **132**, 154104 (2010).
- [78] H. J. Kulik, M. Cococcioni, D. A. Scherlis, and N. Marzari, *Phys. Rev. Lett.* **97**, 103001 (2006).
- [79] A. A. Mostofi, J. R. Yates, Y. S. Lee, I. Souza, D. Vanderbilt, and N. Marzari, *Comput. Phys. Commun.* **178**, 685 (2008).
- [80] G. Pizzi, V. Vitale, R. Arita, S. Blugel, F. Freimuth, G. Geranton, M. Gibertini, D. Gresch, C. Johnson, T. Koretsune *et al.*, *J. Phys. Condens. Matter* **32**, 165902 (2020).
- [81] Q. S. Wu, S. N. Zhang, H.-F. Song, M. Troyer, and A. A. Soluyanov, *Comput. Phys. Commun.* **224**, 405 (2018).
- [82] V. Wang, N. Xu, J. C. Liu, G. Tang, and W.-T. Geng, *Comput. Phys. Commun.* **267**, 108033 (2021).
- [83] U. Herath, P. Tavazde, X. He, E. Bousquet, S. Singh, F. Munoz, and A. H. Romero, *Comput. Phys. Commun.* **251**, 107080 (2020).
- [84] K. Momma and F. Izumi, *J. Appl. Crystallogr.* **44**, 1272 (2011).
- [85] M.-H. Chiu, C. Zhang, H.-W. Shiu, C.-P. Chuu, C.-H. Chen, C.-Y. S. Chang, C.-H. Chen, M.-Y. Chou, C.-K. Shih, and L.-J. Li, *Nat. Commun.* **6**, 7666 (2015).
- [86] V. O. zcelik, J. G. Azadani, C. Yang, S. J. Koester, and T. Low, *Phys. Rev. B* **94**, 035125 (2016).
- [87] C. Xia, J. Du, M. Li, X. Li, X. Zhao, T. Wang, and J. Li, *Phys. Rev. Appl.* **10**, 054064 (2018).
- [88] C. Lei, Y. Ma, X. Xu, T. Zhang, B. Huang, and Y. Dai, *J. Phys. Chem. C* **123**, 23089 (2019).
- [89] X.-R. Hu, J.-M. Zheng, and Z.-Y. Ren, *Front. Phys.* **13**, 137302 (2018).
- [90] Z.-Z. Yan, Z.-H. Jiang, J.-P. Lu, and Z.-H. Ni, *Front. Phys.* **13**, 138115 (2018).
- [91] Y.-Y. Wang, F.-P. Li, W. Wei, B.-B. Huang, and Y. Dai, *Front. Phys.* **16**, 13501 (2021).
- [92] C. Zhao, T. Norden, P. Zhang, P. Zhao, Y. Cheng, F. Sun, J. P. Parry, P. Taheri, J. Wang, Y. Yang, T. Scrace, K. Kang, S. Yang, G.-x. Miao, R. Sabirianov, G. Kioseoglou, W. Huang, A. Petrou, and H. Zeng, *Nat. Nanotechnol.* **12**, 757 (2017).
- [93] T. Norden, C. Zhao, P. Zhang, R. Sabirianov, A. Petrou, and H. Zeng, *Nat. Commun.* **10**, 4163 (2019).
- [94] X. Deng, H. Yang, S. Qi, X. Xu, and Z. Qiao, *Front. Phys.* **13**, 137308 (2018).
- [95] Y. Han, S. Sun, S. Qi, X. Xu, and Z. Qiao, *Phys. Rev. B* **103**, 245403 (2021).
- [96] S. Qi, R. Gao, M. Chang, Y. Han, and Z. Qiao, *Phys. Rev. B* **101**, 014423 (2020).
- [97] S. Qi, Z. Qiao, X. Deng, E. D. Cubuk, H. Chen, W. Zhu, E. Kaxiras, S.B. Zhang, X. Xu, and Z. Zhang, *Phys. Rev. Lett.* **117**, 056804 (2016).
- [98] Z. Li, Y. Han, and Z. Qiao, *Phys. Rev. Lett.* **129**, 036801 (2022).
- [99] Y. Han, Z. Yan, Z. Li, X. Xu, Z. Zhang, Q. Niu, and Z. Qiao, arXiv:2203.16429.